RSC Advances

Facile Fabrication of Highly Efficient Modified ZnO Photocatalyst with Enhanced Photocatalytic, Antibacterial and Anticancer Activity

Journal:	*RSC Advances*
Manuscript ID	RA-ART-03-2016-006774.R3
Article Type:	Paper
Date Submitted by the Author:	02-Jul-2016
Complete List of Authors:	Raza, Waseem; Aligarh Muslim University, Chemistry Faisal, S.; Aligarh Muslim University Owais, M.; Aligarh Muslim University Bahnemann, Detlef W; Leibniz Universitaet Hannover, Institut fuer Technische Chemie Muneer, M.; Aligarh Muslim University
Subject area & keyword:	Nanocatalysis - Catalysis < Catalysis

Facile Fabrication of Highly Efficient Modified ZnO Photocatalyst with Enhanced Photocatalytic, Antibacterial and Anticancer Activity

Waseem Raza[1], Syed Mohammad Faisal[2], Mohammad Owais[2], D. Bahnemann[3], M. Muneer*[1]

[1]Department of Chemistry, Aligarh Muslim University, Aligarh -202002, India
[2] Interdisciplinary Biotechnology Unit, Aligarh Muslim University, Aligarh-202002, India
[3]Institut fuer Technische Chemie, Leibniz Universität Hannover, Callinstrasse 3, D-30167 Hannover, Germany

Abstract

The degradation of organic pollutants in the aqueous environment by using semiconductor photocatalyst has become an attractive process. Of which ZnO being most efficient photocatalyst. But still there are few disadvantages which have to be overcome such as i) The wide band gap of ZnO (3.37 eV) and ii) fast recombination rate of photogenerated electron−hole pair which limits the photodegradation efficiency of bare ZnO photocatalyst. Herein, we report the strategy for the suppression of electron−hole pair recombination rate, extended the absorption edge in the visible region and enhanced the photocatalytic efficiency by introducing rare earth metal as dopant. Therefore, in this paper, we report the fabrication of pure and Er/Nd doped ZnO semiconductor photocatalysts with hexagonal wurtzite structure using sol gel method. The prepared photocatalysts were characterized by standard analytical techniques, such as XRD, SEM-EDS, TEM, FT-IR, XPS, BET, TGA, DTA, DSC, PL, DRS and UV−Vis spectroscopy. The photocatalytic activity of pure and doped ZnO nanoparticles (NPs) was investigated by studying the degradation of two different organic dyes as a function of irradiation time. The results indicate that the photocatalytic activity of doped ZnO was found to be higher than bare ZnO for degradation of dyes. This may be attributed predominantly due to decrease in the recombination rate by the efficient charge separation of photoinduced electron−hole pair as inferred from PL spectra. The results also indicate that parameters such as amount of photocatalyst dose, initial pH and different quenchers play a significant role for degradation of model dyes. This synthesized photocatalyst was recycled four times for degradation of dyes with very little decrease in efficiency. Interestingly, comparative in vitro antibacterial and anticancer potential of the pure and Er/Nd doped ZnO NPs were also investigated against human pathogenic bacterial strains and various human cancer cell lines. The result of our study clearly revealed that Nd doped ZnO NPs

*Corresponding author. (M. Muneer) Tel.: +91-571-2700920 ext. 3365. E-mail address: m.muneer.ch@amu.ac.in; readermuneer@gmail.com

showed better antibacterial as well as anticancer efficacy as compared to pure and Er doped ZnO NPs.

Keywords: Metal doped ZnO, Photocatalysis, dye degradation, Sol gel synthesis and charge separation.

1. Introduction

Water pollution by different sources such as agricultural runoff, phenols, detergents, industrial effluent, dyes, pesticides and other chemical products are major concern to the society all over the world [1]. Due to development of new methods for dyeing, textile, paper and pulp, a large amount of harmful waste containing nonfixed dyes are continuously released into the water system. Most of the dyes contain high degree of aromaticity, substituted with azo (-N=N) and hydroxyl group (-OH) group which are non-biodegradable [2]. These textile dyes are not only polluted water as well as hazardous for health. So it is very important to develop such techniques which are helpful for remediation of such environmental pollutants. Hence, extensive research have been carried to developed innovative techniques such as flocculation−precipitation, oxidation, adsorption, physicochemical, biological and electrochemical treatment for the degradation of dyes/organic pollutant in water bodies. But these methods are not so effective because these methods not completely degrade the pollutants as well as produce secondary pollutants [3]. Hence, it is a vital need to develop a new clean and ecofriendly technique for treating such environmental pollutants [4]. The degradation of organic dyes in aqueous phase by using advanced oxidation processes (AOPs) is an efficient approach. Purification of waste water by using photocatalysis is one of the most widely used application of AOPs [5]. Recently, semiconductor based heterogeneous photocatalysis attracted strong attention for degradation of pollutants via photo-splitting of water using renewable solar energy [1,6,7]. The reactive species generated can also kill microorganism. Many semiconductor based heterogeneous photocatalysts, such as SnO_2, Bi_2O_3, WO_3, TiO_2 and ZnO has been widely used for degradation of organic pollutants [8–10]. Among various semiconductor photocatalysts ZnO and TiO_2 are known to be the excellent material for waste water treatment [11,12]. Although TiO_2 is universally recognized, extensively investigated and widely employed as the most active photocatalyst. In addition, ZnO is also used as a suitable alternative to TiO_2 due to its, high reactivity, more volume to area ratio, large excitation binding energy (60 meV), environmentally friendly nature, low cost and long life span [4,13,14]. ZnO is a n-type II-VI semiconductor and has a

wurtzite structure [15]. However, the practical application of ZnO is restricted to UV-light due to its wide band gap and fast recombination rate of photogenerated charge carrier [16]. Therefore, extensive researches are being carried out for the improvement of electrical and optical properties of bare ZnO. Development of solar light driven ZnO can effectively be carried out by doping with nonmetals, metals, metal oxide, and carbon materials [17–20]. During doping the higher valency rare earth metals ions can replace the Zn^{2+} ion from the ZnO lattice [12,15,21,22]. Recently, doping of ZnO with rare earth metals has attracted much attention due to f orbital that allow adsorption of more pollutants on the catalyst surface and reducing band gap energy which may intern improve the photocatalytic activity. Rare earth metals have good ability to trap the photogenerated charge carrier and reduce the recombination rate, which may increase the photocatalytic activity of doped ZnO [23]. Among them Er & Nd doped ZnO attracted strong attention due to optical intra 4f transition. which can cause an emission at 1.54 μm with minimum loss and its abundance characteristics energy level, tremendous application in infrared and visible region [24]. There are only few reports available on photocatalytic degradation of organic pollutants using rare earth doped ZnO semiconductor. A wide range of methods has been employed for the preparation of doped ZnO photocatalyst, such as autocombustion, co-precipitation, solvothermal processes, precipitation and ball-milling [25–29]. However, these methods are expensive, required complex equipment. Currently, synthesis of metal doped ZnO photocatalyst using sol–gel process has attracted considerable attention because of its acceptable costs, simplicity, no need complex experimental condition, good crystalline quality and easy to handle [30]. This method is also helpful for synthesis of ZnO with different morphologies, various sizes and higher surface area. The photocatalytic activity also depends upon the size and shape of fabricated ZnO. Controlled morphology of ZnO can increase the photodegradation rate of pollutants [31]. Herein, we report the synthesis of pure and Er/Nd doped ZnO NPs using sol gel method. The characterization of synthesized materials was carried out using standard analytical techniques, such as X-ray diffraction analysis (XRD), Scanning electron microscopy (SEM), Electron dispersive X-ray spectroscopy (EDS), Transmission electron microscopy (TEM), UV-Vis spectroscopy, UV-Vis diffuse-reflection spectroscopy (DRS), Fourier transformed infrared spectroscopy (FTIR), Differential thermal analysis (DTA), Thermo gravimetric analysis (TGA), Differential scanning calorimetry (DSC), Brunauer −Emmett −Teller (BET), X-ray photoelectron spectroscopy (XPS) and photoluminescence (PL). The photocatalytic

activity of prepared photocatalyst was tested by studying the degradation of two different organic dyes under visible light illumination. We also performed the antibacterial and anticancer activity of the prepared materials against human pathogenic bacterial strains and various human cancer cell lines.

2. Experimental section

2.1 Reagents and chemicals

Zinc Acetate dihydrate was purchased from Sigma-Aldrich. Reactive Red 241 (RR 241) was supplied by Atul India Ltd. Valsad, Gujrat, India. Triton-X, Nitric acid (HNO_3, 98 wt%), sodium hydroxide (NaOH), isopropanol (IPA), Potassium Iodide (KI) and Ammonium solution were obtained from Merck, while Erbium nitrate hexahydrate, Neodymium nitrate hexahydrate Methylene Blue (MB) were purchased from Central Drug House, India. Benzoquinone (BQ) was obtained from alfa aesar.

2.2. Preparation of pure and doped ZnO NPs

All reagents were of analytical grade and used without further purification. Doped ZnO NPs were prepared by sol gel method using zinc acetate dihydrate as a precursor and Erbium nitrate hexahydrate/Neodymium nitrate hexahydrate as a dopant. In a typical procedure (6 g, 0.023 M) of zinc acetate dihydrate and 5 mL Triton-X was dissolved in 50 mL double distilled water in round bottom flask under vigorous stirring for 60 min at room temperature to form a transparent solution. To the above solution, desired mole percent of dopants in ammonium solution was added drop wise. The solution was stirred continuously at 40 ^{0}C until the formation of a white gel. The obtained gel was aged 24 h, which was filtered and washed thoroughly with water and ethanol. The obtained material was dried at 120 ^{0}C for 2 h in oven and then manually grounded into fine powder and calcinated at 600 ^{0}C for 4 h. The pure ZnO NPs was fabricated by using the same method without addition of dopant solutions. The formation of ZnO NPs can be explained by the chemical reaction given below.

$$Zn(CH_3COO)_2.2H_2O + 4NH_4OH \longrightarrow Zn(NH_3)_4^{2+} + 2CH_3COOH + 6H_2O \quad \text{Eq 1}$$

$$Zn(NH_3)_4^{2+} + 2OH^- \longrightarrow ZnO + 4NH_3 + 2H_2O \quad \text{Eq 2}$$

2.3 Characterization

The X-ray diffraction (XRD) analysis of the fabricated samples were carried out with Shimadzu diffractrometer (model 6100) with Cu Kα radiations (λ = 1.5418 Å) operated at a voltage of 30 KV and current of 15 MA in the 2θ range of 20-80°. A JEOL JSM-6510 scanning electron microscope (SEM) was used to study the surface morphology and

elemental analysis of pure and doped ZnO NPs. The optical properties of the prepared NPs were characterized by using UV-Vis absorption spectroscopy and UV-Vis diffuse-reflection spectroscopy with a Perkin Elmer spectrophotometer ($\lambda = 35$). Fourier transform infrared (FTIR) spectra of the fabricated NPs were recorded in KBr powder as a reference at room temperature using a Perkin-Elmer Spectrum 2 in the range of 400 – 4000 cm^{-1}. Photoluminescence (PL) spectra of the prepared materials were recorded using Hitachi (F-2700). A Xe lamp was used as excitation source during PL study and PL spectra was performed at an excitation wavelength 290 nm. Thermal analysis (TGA/DTA) measurement of the prepared NPs was done by using Shimadzu (model 60H) and DSC by using Shimadzu (model 60). X-ray photoelectron spectroscopy (XPS) was carried out by a PHI VersaProbe II with AES photoelectron spectrometer. The Brunauer −Emmett −Teller (BET) analysis was done using Quantachrome Autosorb Automated Gas Sorption System Instruments.

2.4 In vitro antibacterial studies

2.4.1 Bacterial Strain

The bacterial strains were used for the screening of Gram negative Escherichia coli (American Type Culture Collection (ATCC) ® 25922TM; ATCC, Manassas, VA, USA), Gram positive Listeria monocytogene (Microbial Type Culture Collection Gene Bank (MTCC) ® 657TM; MTCC, IMTECH, Chandigarh, India) and Staphylococcus aureus (ATCC 25923). E. coli strains was cultured in Luria Bertani broth while L. monocytogene and S. aureus were cultured in Brain Heart Infusion broth medium for 12-18 hours at 37 ^{0}C.

2.4.2 Agar well diffusion assay

The antibacterial potential of the pure and doped ZnO NPs were evaluated using agar well diffusion method [32]. The inoculum was prepared by diluting the overnight cultures with sterile normal saline to a 0.5 McFarland standard. The agar petri plates were prepared by spreading the $1x10^7$ CFU/50µL of mature broth culture of specific bacterial strains with the sterile L-shaped glass rod. The well of 8 mm was created in each petri-plate with the help of sterile yellow tips. Various formulation of ZnO suspended in sterile phosphate buffer saline was used to evaluate the antibacterial activity. Experimental procedure was performed under sterile condition using bio-safety level 2 (BSL-2) hoods and petri plates which was incubated at 37 ^{0}C for 12–18 h. The susceptibility of our formulation was determined on the basis of diameter of the zone of inhibition against human pathogenic

strain *E.coli, S. aureus* and *L. monocytogene*. Inhibition zone was measured in triplicates with various forms of ZnO NPs, average of the three were calculated for the antibacterial activity and compared with the reference drug Gentamicin as a control.

2.5 In vitro Cell viability analysis by MTT assay

2.5.1 Cell culture

Human breast cancer cell line (MDA-MB-231), human liver cancer cell line (Hep3B) and human cervical cancer cell line (HeLa) was used in the present study and cell lines were procured from Cell Repository–National Centre for Cell Science, Pune (India). Cell lines were cultured in the Roswell Park Memorial Institute (RPMI) 1640 culture medium supplemented with 10% heat inactivated fetal bovine serum (FBS) and 0.5% antibiotic antimycotic solution (Sigma-Aldrich Co, St Louis, MO, USA) at 37°C in a humidified incubator maintaining 5% CO_2.

2.5.2 MTT assay

The anticancer potential of the pure and Nd/Er doped ZnO NPs were determined using 3-(4, 5-dimethylthiazol-2-y1)-2, 5-diphenyltetrazolium bromide (MTT) assay. MTT is a colorimetric assay, which is based on the ability to cleave the tetrazolium ring of the MTT by mitochondrial dehydrogenase enzyme of the viable cells to insoluble formazan crystals, which deposits in the living cells. This insoluble formazan is then dissolved by addition of a suitable solvent into a purple colored solution. The absorbance of this colored solution can be measured at 570 nm [33].The amount of formazan crystal product is directly proportional to the number of living cells.

2.6 Photocatalytic performance Experiment

The photocatalytic activity of prepared samples was evaluated by studying the of degradation of an aqueous solution of two different organic dyes (RR-241 and MB) under visible light illumination using (500 W) tungsten halogen linear lamp as a light source. Typically, required amount of photocatalyst was added to 200 ml of an aqueous solution of dyes such as RR-241 (14 ppm) or MB (10 ppm) in to the immersion well photochemical reactor. Prior to illumination, the solution was first ultrasoniated for 10 min and then stirred in the presence of photocatalyst in the dark for 15 min to ensure the establishment an adsorption-desorption equilibrium. In order to maintain the temperature ($20 \pm 0.5\ ^{0}C$) of dye solution to minimize the effects of heating, the photoreactor was surrounded by refrigerated flowing water. The zero time reading was given to a blank solution kept in the dark, otherwise treated similarly to the irradiated solution. At a given time interval 5 ml suspension was withdrawn and centrifuged at 4000 rpm for 30 min to

remove the photocatalyst powder completely. The photocatalytic degradation of RR-241 and MB dyes were monitored using a Perkin Elmer (Lamda 35) spectrophotometer.

3 Results and Discussion

3.1 XRD Analysis

The crystal structure of fabricated NPs was investigated by powder X-ray diffraction (XRD) analysis. Fig. 1 displays the XRD patterns of pure and Er/Nd doped ZnO calcinated at 600 ^{0}C for 4 h. The peaks at 31.80, 35.2, 36.9, 47.50, 56.50, 62.80, 66.20, 67.80, 69.10 78.20 could be indexed to (100), (002), (101), (102), (110), (103), (200), (112), (201) and (202) crystal planes of hexagonal wurtzite ZnO ($P6_3mc$, a = 3.1495, c = 5.106) respectively [34,35]. The XRD patterns of doped ZnO also exhibit the same pattern as of pure ZnO indicating product being in pure hexagonal phase. The XRD analysis also indicate that there is no change in the crystal structure upon doping [36]. Furthermore, all diffraction peak were intense and sharp, indicating that the prepared NPs are in crystalline nature without any amorphous phase [4,37]. The average crystallite size of pure and Er/Nd doped ZnO was estimated by Debye Scherer formula:

$$D = \frac{0.9\lambda}{\beta \cos\theta} \quad \text{Eq 3}$$

Where D is the crystallite size, λ is the X-ray wavelength (0.154 nm), θ is the Bragg diffraction angle and β is the full width at half maximum (FWHM). Crystallite size of pure and doped ZnO NPs were calculated using most intense peak (101). Crystallite size of doped ZnO was found to be smaller than that of the pure ZnO as given in table 1. The decrease in the crystallite size of Er/Nd doped ZnO is mainly due to the formation of Er–O–Zn or Nd-O-Zn on the surface of the doped samples, which may hinder the growth of ZnO particle to some degree [15,38].

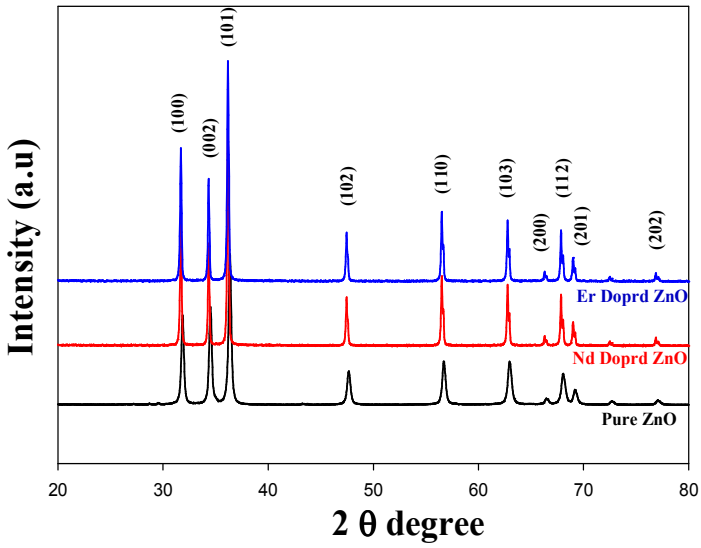

Fig. 1. XRD pattern of pure and Er/Nd doped ZnO NPs.

S. No.	Dopant concentration (Er) / Crystallite size (nm)	Dopant concentration (Nd) / Crystallite size (nm)
1.	00/21.25	00/21.25
2.	1.0/14.21	0.5/13.52
3.	3.0/13.43	1.0/12.32
4.	5.0/12.23	1.5/11.54
5.	7.0/12.12	2.0/10.23
6.		2.5/9.45

Table 1. Crystallite size of pure and doped ZnO NPs with different dopants concentration.

3.2 FTIR Analysis

To confirm the nature of reaction intermediate and identification of various functional group which participate in the formation of ZnO NPs, FTIR analysis was carried out in

the wavenumber range from 400 to 4000 cm^{-1} using KBr powder at room temperature as shown in Fig. 2. The peaks below 500 cm^{-1} was assigned to stretching vibration of Zn–O [39]. The stretching vibration corresponding to bond between dopant and Oxygen (Nd/Er–O) appears between 948-1113 cm^{-1} [15,40,41]. A sharp absorption band at 1623 cm^{-1} in higher energy region was ascribed to O-H bending vibration [39]. The ZnO surface contains hydroxyl groups and water molecules either chemisorbed or physiorbed was confirmed by the broad absorption band at around 3440 cm^{-1} [42]. The peak at 2920 and 2842 cm^{-1} corresponding to -CH- stretching band which belong to Triton-X [39,43]. The sharp peak at 2332 cm^{-1} gave the information of atmospheric CO_2 absorbed on the metal cation [15,44].

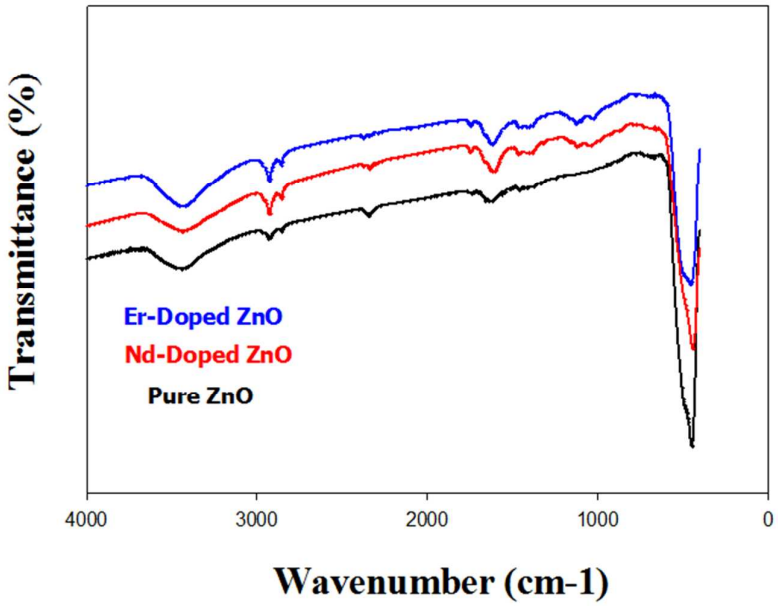

Fig. 2. FTIR Spectra of pure and Er/Nd doped ZnO NPs.

3.3 Optical properties and band gap

The optical characterization of synthesized material was done using UV−Vis diffuse reflectance spectroscopy (DRS). The DRS is a good technique for examine the light harvesting ability of synthesized hexagonal semiconductor photocatalysts [45,46]. Fig. 3 presents the DRS spectra of fabricated pure and Er/Nd doped ZnO NPs. A strong absorption at 372 nm in the UV region corresponding to pure ZnO may be due to band to band transition [47,48]. The Er/Nd doped ZnO NPs showed the broad absorption near 452 and 465 nm in the visible region. The band gap energy of pure and Er/Nd doped ZnO NPs was calculated by equation 4 [49].

$$\alpha h\nu = A(h\nu - Eg)^{n/2} \quad \text{Eq 4}$$

Where α, ν, Eg, and A are the absorption coefficient, light frequency, band gap, and a constant, respectively. Moreover, n depends on the characteristics of the transition in a semiconductor for direct transition n = 1and for indirect transition n = 4. The value of n for ZnO was 1 due to direct transition [50]. The band gap energy of pure and doped ZnO NPs is calculated from the plot between $(\alpha h\nu)^2$ versus photon energy (hν). As seen from the inset Fig 3 the band gap of pure ZnO was found to be 3.3, while the band gap of Er and Nd doped ZnO was evaluated to be 2.74 and 2.66 respectively. These results are consistent with the previous results [51–55]. The band gap energy was found to be decreases from 3.37 to 2.66 after doping it may be due to increased defects introduced by Er and Nd doping or substitutional impurity located in the lattice position of ZnO [56]. A higher defect makes the electronic transitions easy from the filled valence band to the energy level of the defect more probable than the transitions to the conduction band [57].

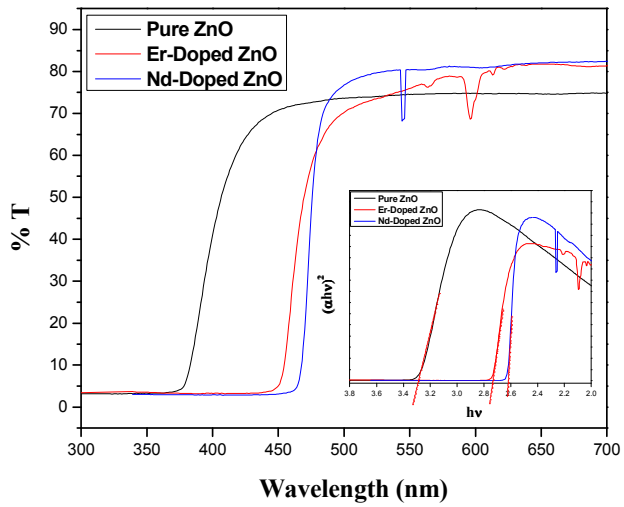

Fig. 3. U V-vis diffuses reflectance (DRS) spectra and the inset of the Fig shows the plots of $(\alpha h\nu)^2$ vs photon energy (hν) for pure and Er/Nd doped ZnO NPs.

3.4 Material Morphology analysis (SEM-EDS and TEM)

The morphologies of pure and Er/Nd doped ZnO NPs calcinated at 600 ^{0}C for 4 h were investigated by SEM as shown in Fig.4 (a-c). From the Figs, we can see that the pure and

Er/Nd doped ZnO form hexagonal rod-like structure with the aggregation of prepared ZnO NPs possess non-uniform morphology lying on top of one another. After doping with different concentration of Er and Nd the surface becomes rough, implying the deposition of Er and Nd on the surface of ZnO. Dopants also decrease the aggregation of NPs. The grain size of doped NPs was gradually decreased as the dopants concentration increased. As the crystallite size decreases upon doping the aggregation of NPs also decreases which lead to increase the surface area and therefore photocatalytic reaction sites also increases, which is favorable to increase the photocatalytic activity of fabricated NPs for degradation of target pollutants.

The percentage of doping in ZnO NPs was confirmed by EDS analysis, the results are illustrated in Fig. 5 (A&B) which indicate the existence of Nd and Er metal ions in the ZnO lattice. The atomic ratio Nd and Er in ZnO was measured from EDX and found to be 1.75% and 4.55% respectively. Figure also shows the presence of Zn, O, Er and Nd demonstrating that Erbium and Neodymium ions are successfully doped into the ZnO NPs.

The surface morphology and particle size of pure and doped ZnO NPs was further analyzed by TEM as shown in Fig. 6 (A&B). TEM images of prepared ZnO NPs clearly indicate the hexagonal rod like structure. It can be seen from the figures that the average particle size of doped NPs was found to 9 to 30 nm. Small particle on the surface may be due to presence of dopants.

(A)

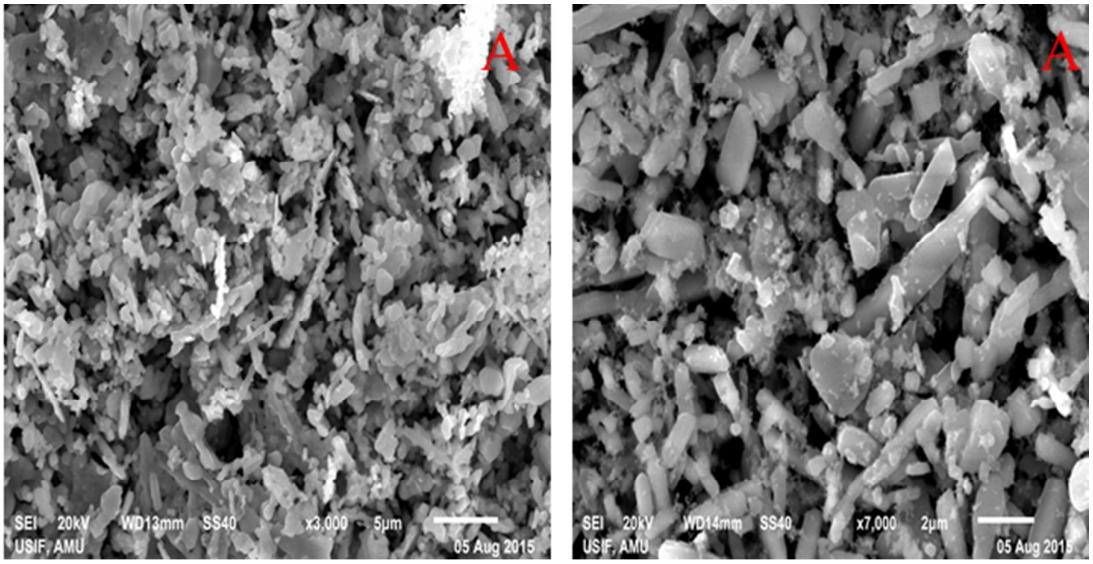
A
SEI 20kV WD13mm SS40 x3,000 5μm
USIF, AMU
05 Aug 2015
A
SEI 20kV WD14mm SS40 x7,000 2μm
USIF, AMU
05 Aug 2015

(B)

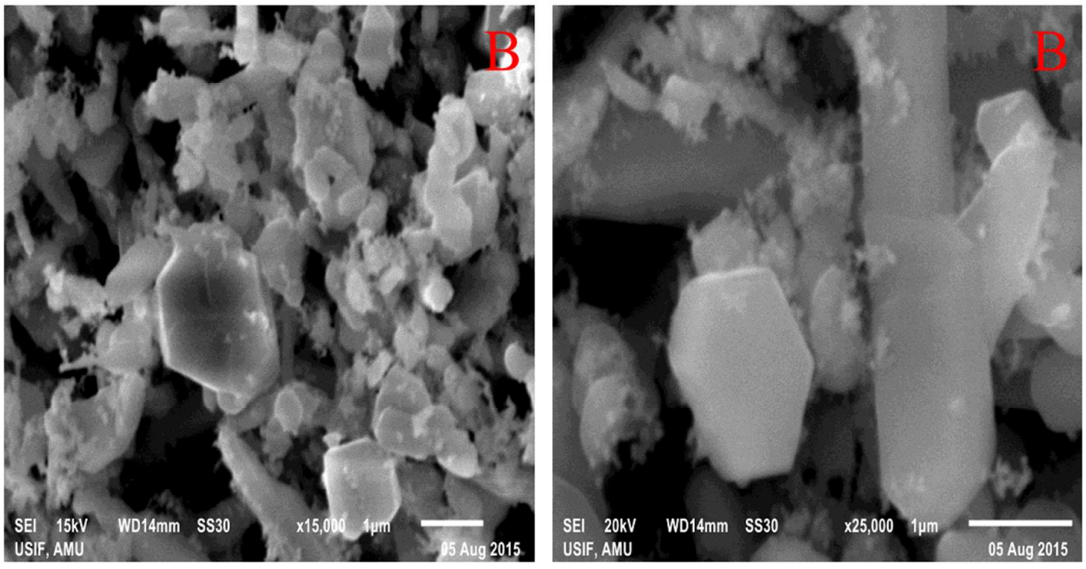
B
SEI 15kV WD14mm SS30 x15,000 1μm
USIF, AMU
05 Aug 2015
B
SEI 20kV WD14mm SS30 x25,000 1μm
USIF, AMU
05 Aug 2015

(C)

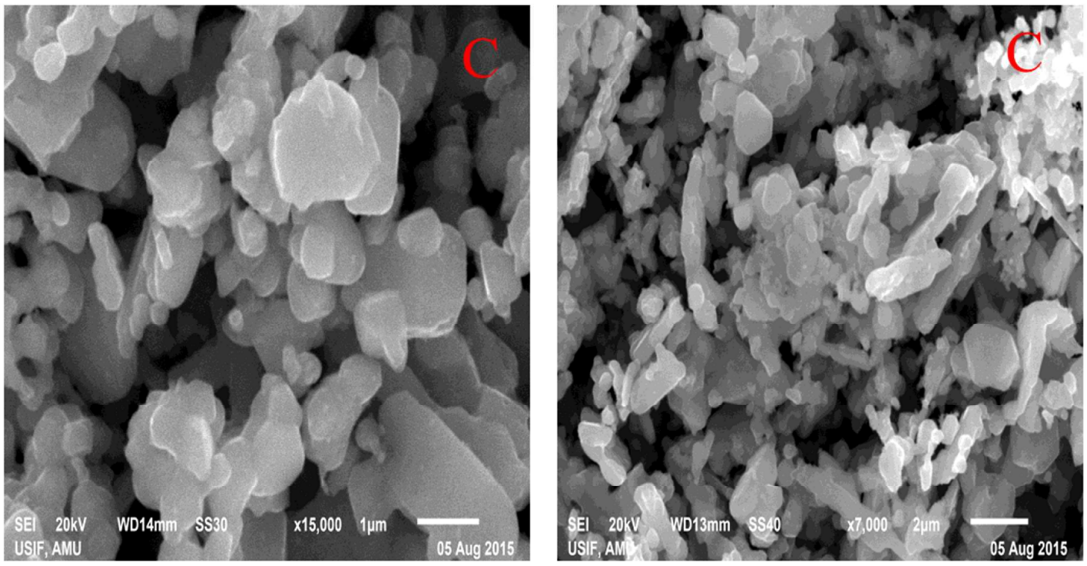

Fig. 4 (a-c). SEM image of (A) pure ZnO (B) Er-doped ZnO and (C) Nd-doped ZnO NPs.

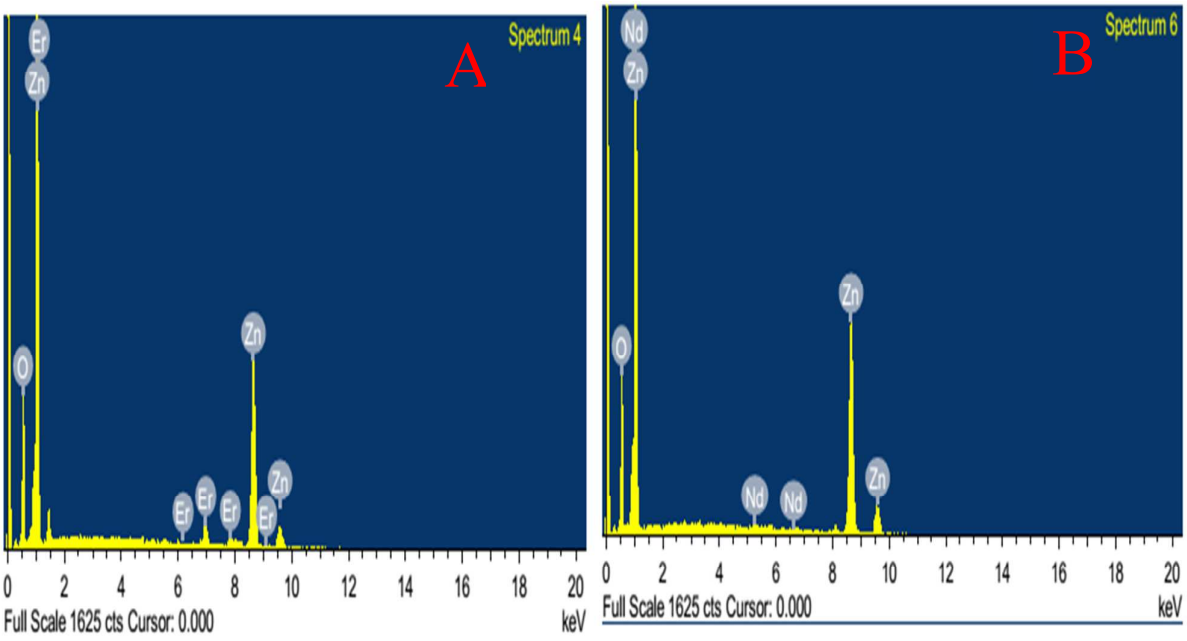

Fig. 5 (A & B). EDS image of (A) Er-doped ZnO and (B) Nd-doped ZnO NPs.

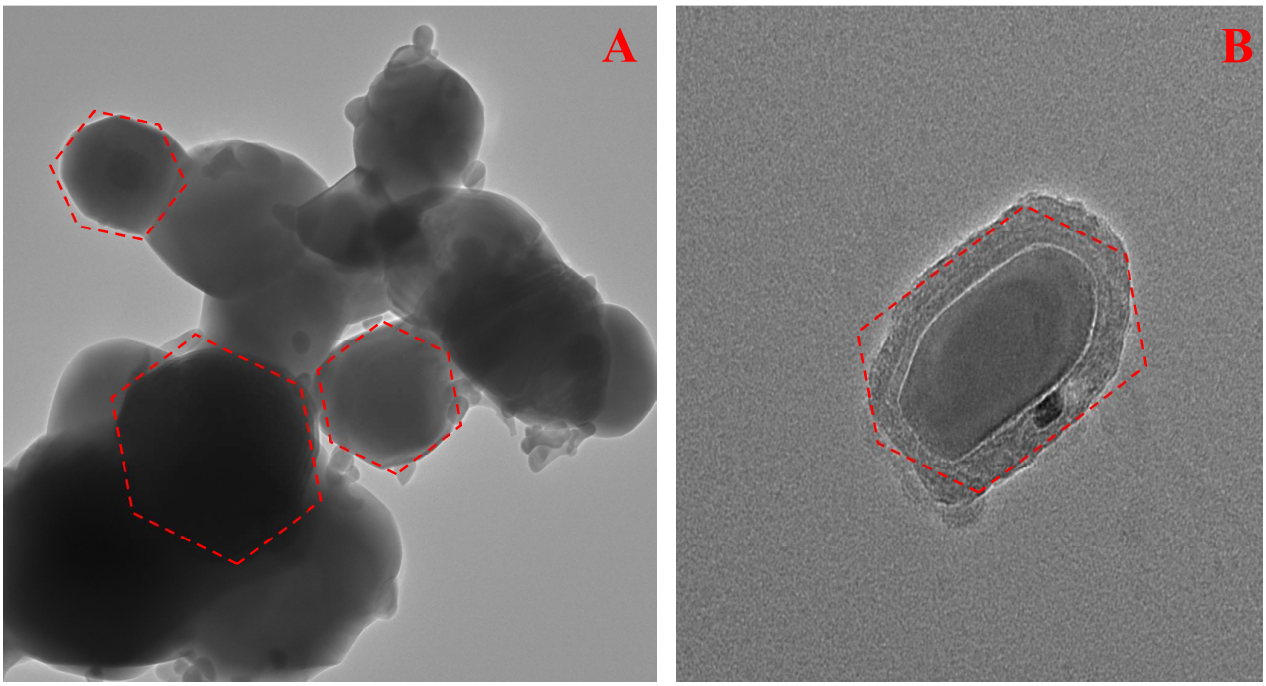

Fig. 6 (A & B). TEM image of (A) Er-doped ZnO and (B) Nd-doped ZnO NPs.

3.5 X-ray photoenergy spectroscopy (XPS)

To further obtain more accurate information regarding doped ZnO, we employed X-ray photoenergy spectroscopy (XPS) analysis to examine the chemical composition and oxidation state of synthesized ZnO NPs. The wide survey scan spectra of Nd and Er doped ZnO NPs are presented in Fig 7 (A & B) respectively, which indicate the presence of only Zn, O, C, Nd and Er elements. The obtained binding energies were corrected by using C 1s 282.8eV as the reference. It could be seen from the [Fig 1S (A) SI] that the peaks appear at 1020 and 1042 eV, are in good agreement with the binding energy value of Zn 2p and ascribed to core level of Zn $2p_{3/2}$ and $2p_{1/2}$ respectively, which indicate the formation of Zn-O bond and also reveal the oxidation of Zn^{2+} in bound ZnO [58–61]. The energy difference between two peaks is 22 eV, which agreed well with standard value i.e 22. 97 eV [60]. The absorption at 530.6 and 532.4 eV are due to lattice oxygen and chemisorbed oxygen (OH) caused by the surface hydroxyl respectively in wurtzite ZnO as shown in [Fig 1S (B) SI] [61,62]. [Fig 2S (A) SI] display the peak at 978.2 and 984.3 eV corresponding to Nd $3d_{5/2}$ and $Nd_{3/2}$ respectively, which reveals that Nd exist as +3 oxidation state in Nd doped ZnO [62]. The peaks positions of Nd3d are closely related to the value of Nd_2O_3 in literature data, which suggest that Nd substitute the Zn [63,64]. [Fig 2S (B) SI] indicate the two binding energy peaks at 184.3 and 188.1 eV corresponding to

$4d_{5/2}$ and $4d_{3/2}$ respectively of Er^{3+} ion in ZnO [65–67]. Based on both the XRD and XPS results, the Nd and Er dopants are successfully incorporated into ZnO lattice.

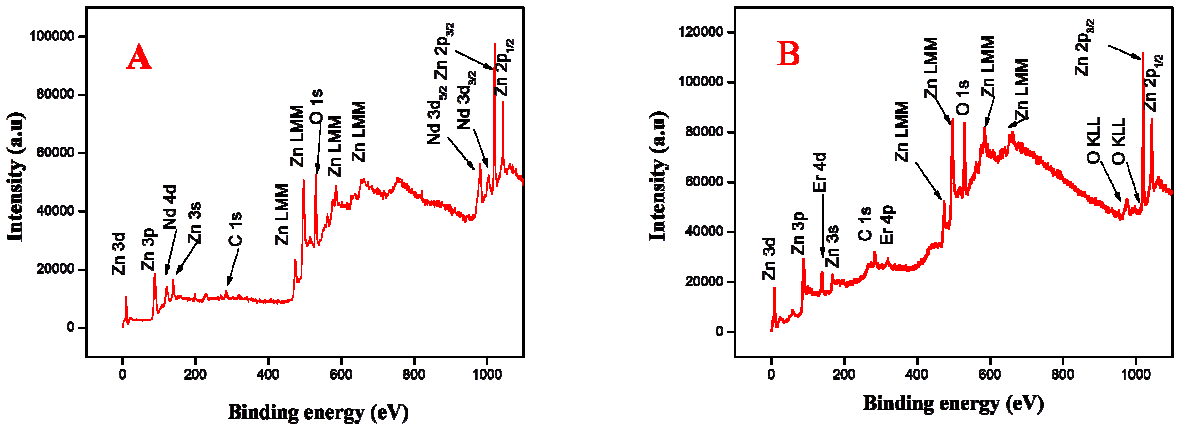

Fig. 7. XPS spectra of **(A)** Nd and **(B)** Er-doped ZnO NPs.

3.6 BET analysis

The BET surface area pore diameter and pore volume of synthesized pure and Er/Nd doped ZnO NPs were examined using nitrogen adsorption–desorption and Barrett–Joyner–Halenda (BJH) analysis at liquid nitrogen. The nitrogen adsorption – desorption isotherms (Fig 3S, SI) showed Type III hysteresis loop shape according to the IUPAC classification. The BET surface, pore diameter and pore volume of pure and 2.0% Nd and 5.0% Er doped ZnO NPs are given in Table 2. The BET surface area of 2% Nd doped was found to higher than either pure ZnO 5.0% Er doped ZnO.

Parameter	Pure ZnO	5% Er-doped ZnO	2% Nd-doped ZnO
BET surface area (m^2/g)	38.23	64.65	73.22
Pore volume (cm^3/g)	0.312	0.332	0.381
Pore Diameter D (nm)	12.67	15.78	19.34

Table 2. BET surface area, pore volume and pore diameter of pure and Er/Nd doped ZnO NPs.

3.7 Photoluminescence (PL) spectroscopy

Photoluminescence (PL) study is well-known powerful technique for investigate the effects of impurity, efficiency of charge carrier trapping, and predict the photocatalytic efficiency of a semiconductors photocatalyst. The PL spectrum of ZnO NPs originates from irradiative recombination of excited or photoinduced charge carriers. The electron and hole play a great role in the deciding the photocatalytic activity of semiconductor photocatalyst. The photocatalytic activity decreases when an electron and hole recombine to emit a photon [68–70]. Therefore, the photocatalytic activity of lower PL spectra would be higher. The PL intensity of ZnO decreases upon doping of Er and Nd as shown in Fig 8. Hence, recombination rate decreases by the efficient charge separation of photoinduced electron−hole pair. The PL spectra of Nd doped ZnO NPs show the lowest intensity peak among all. Therefore, photocatalytic performance of Nd-doped ZnO would be higher than pure and Er doped ZnO. The room temperature PL spectra of pure and Nd/Er-doped ZnO NPs were recorded with irradiation of Xe lamp under an excitation wavelength of 290 nm. It could be seen from the figure that pure and doped ZnO NPs reveal an ultraviolet (UV) emission band at approximately 329, 345 and yellow emission band around at 585 nm. Generally the UV emission band is due to the near band-edge emission (NBE) and the yellow emission in the visible region may be attributed by deep level emission (DLE). The UV emission was ascribed to the free recombination of photogenerated electron in the conduction band and hole in the valence band [71]. The DLE emission in the visible regions would arise due to the intrinsic or extrinsic defects in ZnO NPs.

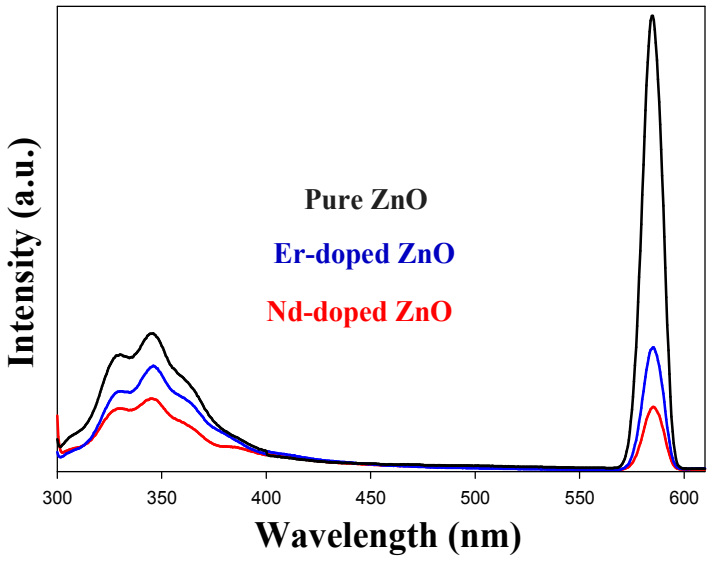

Fig. 8. The PL spectra of pure and Er/Nd doped ZnO NPs.

3.8 Thermal analysis (TGA, DTA and DSC)

To investigate the thermal stability of pure and Nd/Er doped ZnO, thermo gravimetric analysis (TGA), differential thermal analysis (DTA) and differential scanning calorimetry (DSC) were carried out in nitrogen atmosphere. The total weight loss i.e 1.653% was observed for pure ZnO NPs in the temperature range from 100 to 800 ^{0}C (Fig. 4S, SI) and shows good thermal stability upto 100 ^{0}C. In contrast to this Er-doped ZnO NPs display the loss of 4.453% weight (Fig. 5S, SI) in the range of 100 to 800 ^{0}C. The Nd-doped ZnO NPs exhibit a total weight loss of approximately 1.476% in the range of 100 to 800 ^{0}C (Fig. 6S, SI). The initial weight loss for all NPs between 100 to 500 ^{0}C was caused by the evaporation of physically or chemically adsorbed water and hydroxide molecules [72]. The weight loss above 500 ^{0}C might be due to conversion of ZnO into crystalized wurtzite ZnO [15].

The DTA curve of pure and Nd/Er doped ZnO NPs are shown in Fig. 9. The DTA plot revealed three main step of weight loss. The first step from 70 to 300 ^{0}C was ascribed to the removal of free water and weight loss in the second step from 300 to 500 ^{0}C may be due to decomposition of bound water and hydroxyl group. Finally, the weight loss above 500 ^{0}C was due to the crystallization of ZnO [73].

The DSC analysis of pure and doped ZnO NPs heated at 20 ^{0}C / minute from 30 to 550 ^{0}C is given in (Fig. 7S, 8S and 9S, SI). From DSC curve, four endothermic peaks were found at 50, 428, 367 and 393 ^{0}C respectively. The peak at 50 ^{0}C for all NPs indicates the evaporation of adsorbed water molecules. The peaks at 428, 367 and 393 ^{0}C ascribed to crystal transformation from cubic to the wurtzite ZnO [74].

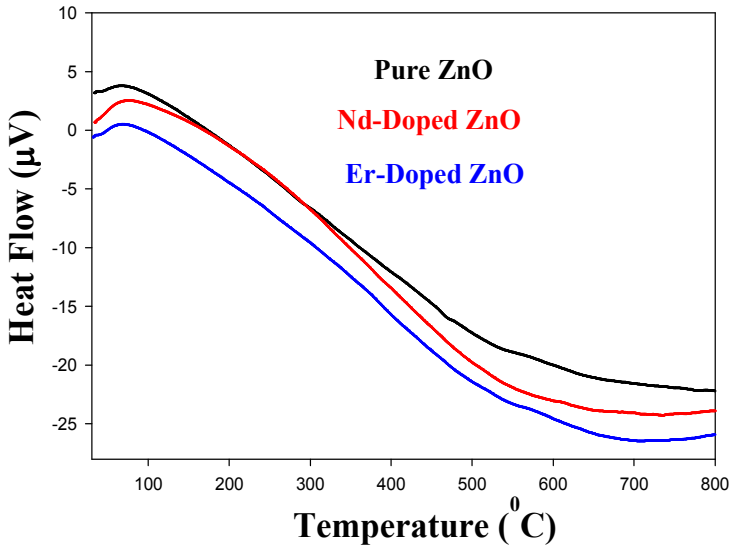

Fig. 9. DTA Plot of pure and Er/Nd-doped ZnO NPs.

3.9 Cytotoxicity and antibacterial activity

In vitro result of the agar well diffusion susceptibility test revealed that Nd-doped ZnO NPs showed better antibacterial activity as compared to pure and Er-doped NPs. Moreover, it was observed that Nd-doped ZnO NPs have shown nearly equivalent bactericidal potential as compared to standard drug Gentamicin, while pure and Er-doped NPs have shown admirable bactericidal potential against gram negative as well as gram positive pathogenic strains. The presence of Zone of Inhibition by the various ZnO NPs against bacterial strains clearly indicated the bactericidal potential of the NPs. Bar graph and zone of inhibition are presented in the Fig.10.

Cytotoxicity effect of pure and Nd/Er-doped ZnO NPs was examined in hela, hep3B and MDA-MB-231 cells by using 3-(4,5-dimethylthiazol-2-y1)-2,5-diphenyltetrazolium bromide (MTT) assay. Cells were placed in a flat bottom 96-well plate at a density of $5x10^3$ cells/well and allowed to grow for 24 hours at 37 ^{0}C. After incubation for 24 hours at 37 ^{0}C, the culture medium was then replaced with the 100 µL fresh medium containing increasing concentration of pure and Nd/Er doped ZnO NPs. The cells were incubated for 48 hours and cell viability was measured by adding 20µL of MTT dye (5mg/mL in phosphate-buffered saline) per well. The plates were incubated for further 4 hours and thus; formazan crystals formed due to reduction of dye by viable cells in each well which were dissolved in 200µL dimethyl sulfoxide (DMSO). The absorbance

was recorded in an ELISA plate reader (iMARK Microplate Absorbance Reader, Bio Rad, California, USA) at 570 nm. The absorption values were expressed as percent cell viability compared with untreated control group considered as 100% viable. The results indicate that there is decrease in cell metabolic activity of all targeted cells with increasing concentration of ZnO NPs. It can be seen from the Fig. 11 that MDA-MB-231 cell show higher damage compared to other two cells. This showed that the MDA-MB-231 cell lines were more sensitive to the cytotoxic effects of ZnO NPs. At 512 uM concentration the toxicity of Nd-doped ZnO NPs was found to be higher than pure and Er-doped ZnO NPs.

Several studies have been reported in literature that an increase in in-vitro cytotoxicity and antibacterial activity with increasing pure and doped hexagonal ZnO rod may be due to i) gathering of NPs in cytoplasm or accumulation on the bacterial surface which disturbed the cellular function and membrane function, ii) generation of reactive oxygen species (ROS) such as hydroxyl radicals, hydrogen peroxide and super oxides which react with cell content such as protein lipid DNA to cause cell death [75–77].

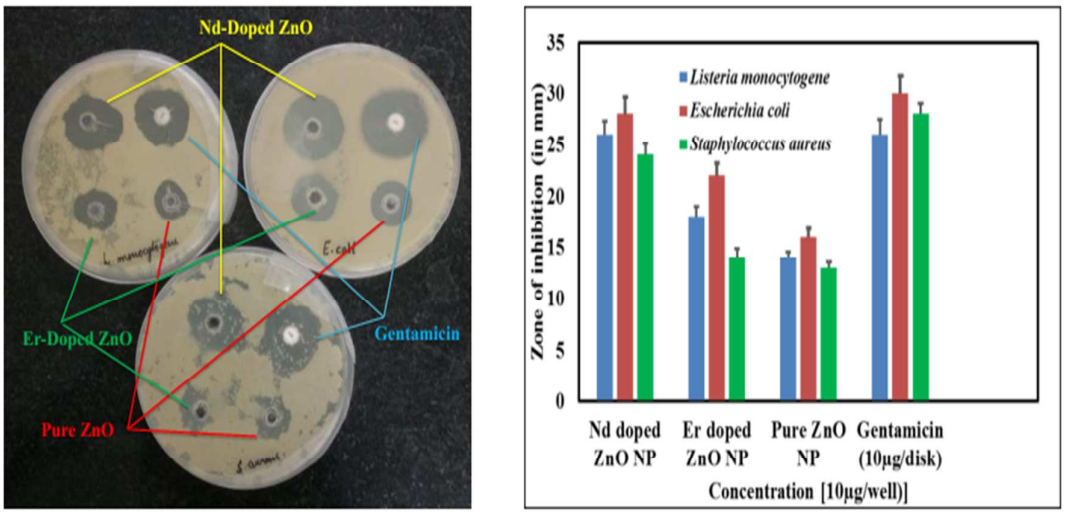

Fig. 10. Bar graph showing diameter of the zone of inhibition (in mm) produced by pure and ND/Er-doped ZnO NPs against *E. coli*, *S. aureus* and *L. monocytogene.*

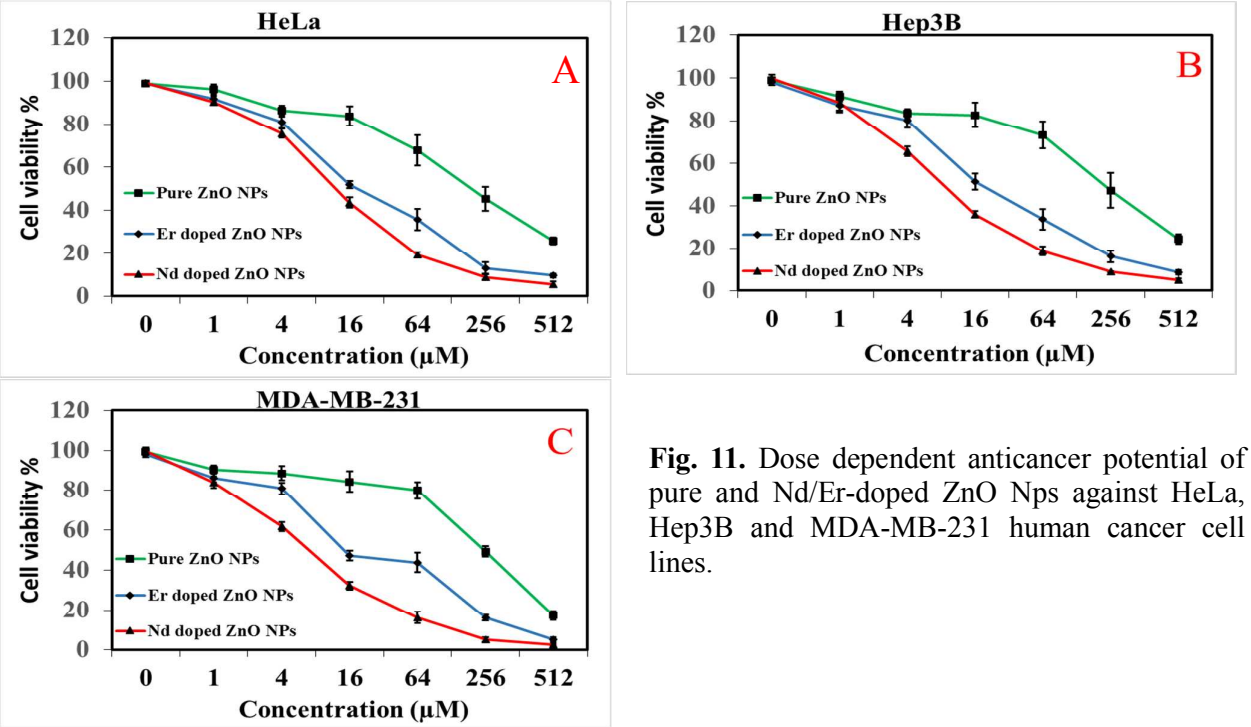

Fig. 11. Dose dependent anticancer potential of pure and Nd/Er-doped ZnO Nps against HeLa, Hep3B and MDA-MB-231 human cancer cell lines.

3.10 Photocatalytic activity

The photocatalytic degradation of two different chromophoric dyes such as MB and RR-241 that are typical organic pollutants discharged by textile industries after used was chosen to evaluate the photocatalytic efficiency of pure and doped ZnO NPs under visible light illumination. The characteristic absorption of MB and RR-241 observed at 663 & 542 nm was used to monitor the photocatalytic performance of pure and doped ZnO NPs. The control experiments indicate that MB and RR-241 were resistant to degradation during irradiation without photocatalyst. However, little degradation of both dyes was observed in presence of photocatalyst in dark due to adsorption of dyes on the catalyst surface. Therefore, both catalyst and light are needed for effective decomposition of dyes. All prepared samples were able to degrade the both dyes under investigation, as observed from the decrease in the characteristic absorbance and decolorization indicating the loss chromophoric groups of dyes and conversion into small aromatic intermediates. Nd & Er doped ZnO NPs exhibit higher activity than pure ZnO under visible light illumination. The results indicate that photocatalytic activity of doped ZnO improved by introducing Er and Nd metal ions into the lattice of ZnO.

In a typical experiment an aqueous solution of MB (10 ppm, 200 mL) or RR-241 (14 ppm, 200 mL) were illuminated in an immersion well photoreactor with a visible

lamp in the presence of pure or desired amount of Er/Nd doped ZnO NPs under constant stirring and bubbling of atmospheric oxygen. Fig. 12 (A&B) display that 100% and 78.6% decomposition of MB and RR-241 dyes take place after 10 min in the presence of 2.0% Nd & 5.0% Er doped ZnO NPs respectively.

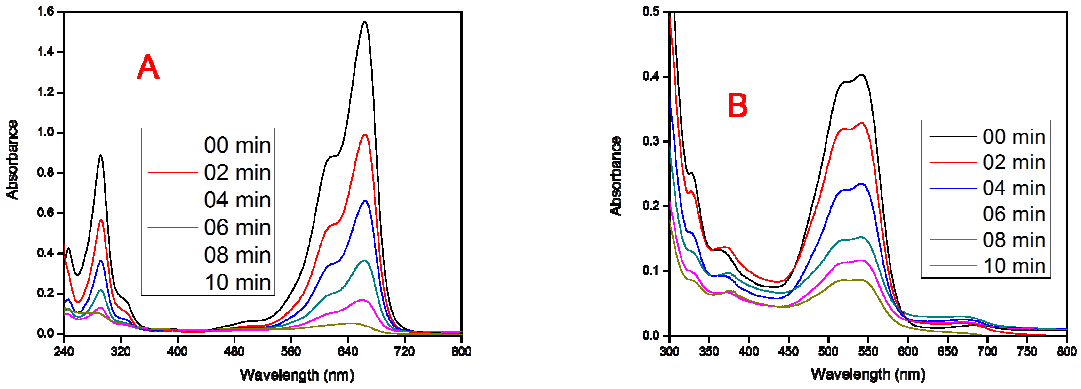

Fig. 12 (A). Change in the absorbance of an aqueous solution of MB (λ_{max} = 663) in the presence of 2.0% Nd-doped ZnO NPs. (**B)** Change in the absorbance of an aqueous solution of RR-241 (λ_{max} = 542) in the presence of 5.0% Er-doped ZnO NPs at different time interval during irradiation under visible light.

To compare the photocatalytic performance of pure and different mole % doped ZnO more precisely, we plotted (C)/(C_0) Vs irradiation time versus for degradation of MB & RR-241 and the results are depicted in Fig. 13 (A&B). The results indicate that the doped NPs presented enhanced photodecomposition of dyes as compared to bare ZnO and the photocatalytic activity significantly increases with increasing the dopant percentage up to 2.0% (Nd) and 5.0% (Er). Further, increase in dopant percentage lead to decrease in degradation of both dyes. However, 30.7% and 19.4% degradation of MB RR-241 dyes takes place over pure ZnO after 10 min due to dye-sensitized mechanism.

To understand the photodegradation of dyes more accurately and quantitatively, we performed kinetics for degradation of dyes in the presence of pure and doped ZnO NPs. The plot of ln(C/C_0) versus irradiation time (t) [as shown in (Fig. 10S (A&B)], for MB (2.0% Nd) and RR-241 (5.0% Er doped ZnO NPs) indicate a good liner fit and the all R^2 (correlation coefficients) values were found to higher than 0.9, which demonstrate that the photodegradation of MB and RR-241 by prepared NPs follow a pseudo-first-order

kinetics and the slope of the linear curve could be considered as the rate constant $k_{apparent}$. The ln C_0/C Vs irradiation time using all prepared ZnO NPs for degradation of MB & RR-241 under visible light illumination is given in Fig. 13 (C&D). The results indicate that the kinetic rate of MB & RR-241 catalyzed by Er and Nd doped ZnO enhanced with increasing the Er and Nd concentration and the Nd (2%) and Er (5%) doped ZnO display the highest photodegradation rate. Further, increase in dopant percentage lead to decrease in degradation of both dyes. The calculated $k_{apparent}$ values of the synthesized NPs are listed in Tables 1S & 2S respectively.

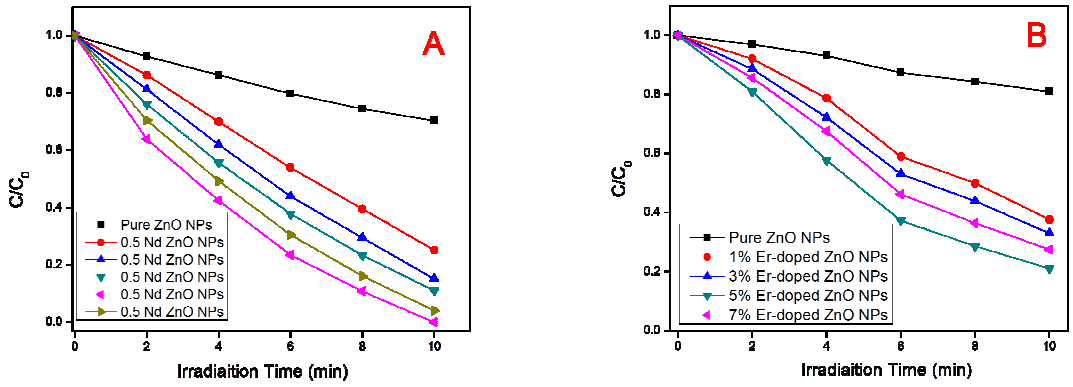

Fig. 13 (A & B). Change in concentration of MB and RR-241 in the presence of pure and different % of Nd and Er doped ZnO NPs respectively under visible light irradiation.

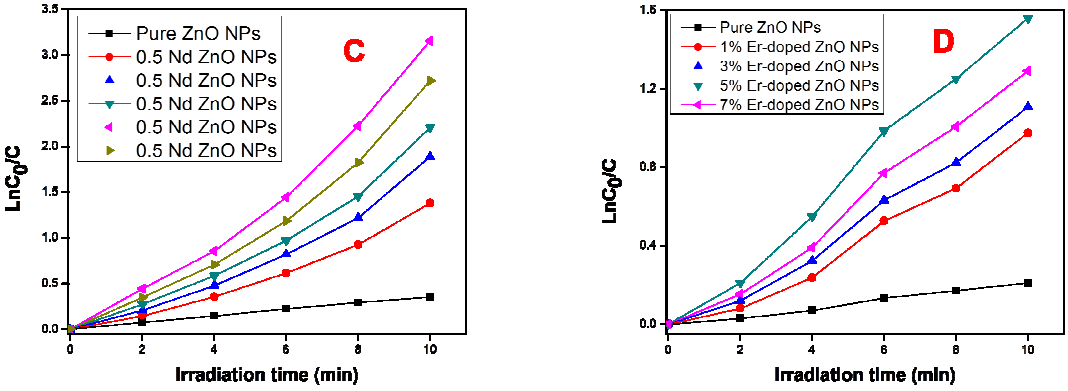

Fig. 13 (C & D). kinetic study of degradation of Mb and RR-241 in the presence of pure and different % of Nd and Er doped ZnO NPs respectively under visible light irradiation.

3.10.1 Effect of different operational parameters on the degradation of dyes

The efficiency of pure and doped catalysts were investigated by degradation of two different chromophoric dyes such as MB (cationic dye) and RR-241 (anionic dye) at other optimum condition under visible light illumination with continuous purging of air. The percentage degradation (η) of dyes was calculated using following equation (5)

$$\eta = \frac{C_0 - C}{C_0} \times 100\% \quad \text{Eq 5}$$

Where C_0 is the initial concentration and C is the concentration at particular time (t).

Fig. 14 (A&B) presents the % degradation of MB and RR-241 over pure and different percent of Nd and Er doped ZnO NPs respectively under 10 min illuminations. It was estimated from the results that the degradation of MB and RR-241 over Nd doped ZnO NPs follow the degradation order as Nd(2%)ZnO > Nd(2.5%)ZnO >Nd(1.5%)ZnO > Nd(1.0)ZnO > Nd(0.5)ZnO > ZnO. The degradation of MB and RR-241 over Er doped ZnO NPs follow the degradation order as Er(5%)ZnO > Er(7%)ZnO >Er(3%)ZnO > Er(1.0)ZnO > ZnO. The degradation efficiency of MB & RR-241 reaches 100% & 89.5% over (2%) Nd and 87.2%, and 78.6 over (5%) Er doped ZnO NPs after 10 min respectively.

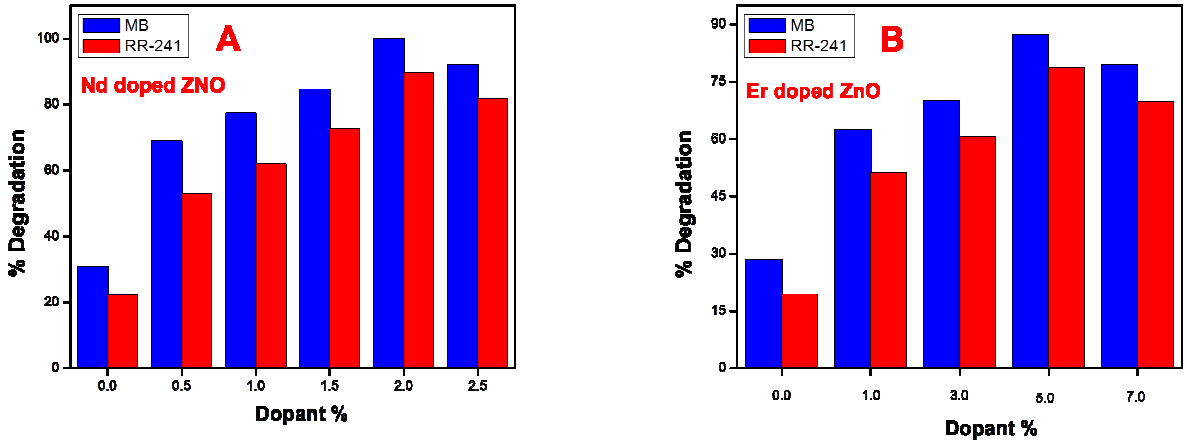

Fig. 14 (A&B). Comparative study for degradation of MB and RR-241 in presence of Nd and Er (with varying dopant %) respectively under visible light irradiation.

The photocatalytic activity of prepared materials were found to increase as the molar ratio of dopant increases from 0 to 2.0% in case of Nd and 0 to 5% in case of Er

doped ZnO NPs. This may be attributed that under visible light illumination dopants act as scavenger to trap the electron and prevent the electron hole recombination rate. The 4f electron transitions of dopants lead to enforce of the optical adsorption of ZnO and also support the charge carrier separation. The degradation efficiency was found to increase as the dopant percentage increases up to 2% Nd and 5% Er doped ZnO NPs and then decreases, suggesting that 2% Nd and 5% Er doped ZnO NPs could be more efficient for achieving high degradation efficiency due to more charge separating ability. Therefore, a precise amount of dopant could be critical for getting high photocatalytic activity [78]. The presence of Nd^{3+} and Er^{3+} ions on the surface of ZnO may promote the following reactions.

$$Nd/Er^{3+} + e^{-} \longrightarrow Nd/Er^{2+} \qquad \text{Eq 6}$$

$$Nd/Er^{2+} + O_2 \longrightarrow Nd/Er^{3+} + O_2^{\cdot -} \qquad \text{Eq 7}$$

Further increase in dopant percentage lead to decrease in the efficiency of photocatalyst may be due the fact that at higher dopant concentration 7.0 % (Er) and 2.5% (Nd) there is occurrence of multiple trapping of charge carriers hence, the recombination of photogenerated electron–hole pair becomes easier and fewer charge carrier will reach the surface to initiate the degradation of the dye, causing reduction in photocatalytic degradation efficiency of photocatalysts. In addition, at high dopant percentage the blocking of light rays or shadowing effect was observed. The turbidity of powder takes place due to aggregation of the catalyst particles, which decreases the penetration depth of light. The aggregation of ZnO powder covers the part of photosensitive surface thereby decreasing the number of surface active sites, which lead to decrease in the photocatalytic activity of the photocatalyst due to an increase in the number of electron−hole recombination centers [79]. Similar results have also been reported in the literature [15,80–84].

In order to optimize the photocatalyst dose, we performed the experiment at different loading of dopants (0.5 to 2.0 g/L) to ensure the use of minimum required amount of catalyst under for highest degradation of dyes. As shown in Fig 11S (A&B), the % degradation of RR-241 and MB increases with increase in catalysts dose from 0.5 to 1.5 g/L (Nd) & 0.5 to 1.0 g/L (Er) doped ZnO NPs and then the % degradation of dyes decreases. The initial increase in the % degradation may be due to increase in total active

surface area, availability of active sites on the catalytic surface and the penetration of visible light. However, at a higher catalyst dose the decrease in % degradation may be due to less visible light penetration and decrease in surface area because of agglomeration of particle. Therefore, less photons may reached to the active surface sites of catalysts [85,86]. Hence, all the experiments were carried out at optimal catalyst loading.

The pH of reaction mixture plays an important role for degradation of dyes because it determines surface charge properties of the catalyst, adsorption/desorption of dyes on the surface of catalyst, charges on dye molecules. Therefore, it is important to study the degradation of dyes at varying pH values of the reaction mixture. In order to see the role of pH on the decolorization of MB and RR-241 we performed experiments at different pH values varying from 4 to 10 using 5.0% Er and 2.0% Nd-doped ZnO NPs. The pH of the reaction mixture was maintained before irradiation by adding an aqueous solution of either HNO_3 or NaOH. The effect of pH on degradation of MB and RR-241 was studied analogous experimental conditions. Fig. 12S (A) shows the change in % degradation Vs pH value (4.0 to 10) for degradation of MB in the presence of 2.0% Nd doped ZnO, whereas, Fig. 12S (B) shows the change in % degradation Vs pH value (4.0 to 10) for degradation of RR-241 in the presence of 5.0% Er doped ZnO. It could be seen from the Fig.12S (A) that the decomposition of MB dye increases upon increase in pH from 4 to 7.8 and a further increase in pH lead to decrease in MB degradation. The degradation of RR-241 increases with increase in pH from 4 to 8.6 and further increase in pH lead to decrease in degradation of RR-241 dye as shown in Fig 12S (B). The rate of decomposition of dyes depends on adsorption of dyes on the surface of ZnO NPs. However, adsorption of dyes depends upon the ionic structure of dyes and point charge value of ZnO. Since the zero point charge for doped ZnO (pH_{zpc}) is about 8.3 [23]. The surface of catalyst remains positively charged below pH_{zpc} whereas the catalyst surface is negatively charged above pH_{zpc} according to following equations 9 and 10 respectively.

$$ZnO\text{-}OH + H^+ \longrightarrow ZnOH_2^+ \text{ (+ve at pH< } pH_{zpc}) \quad \text{Eq 8}$$

$$ZnO\text{-}OH + OH^- \longrightarrow ZnO^- + H_2O \text{ (-ve at pH >} pH_{zpc}) \quad \text{Eq 9}$$

The results indicate that the degradation of both dyes was found to increase with the increase in pH from 4 to 7.8 in case of MB and 4 to 8.6 in case of RR-241 and a further increase in pH lead to decrease in degradation of both dyes. Highest efficiency observed at pH 7.8 (in case of MB) and 8.6 (in case of RR-241) may be due to the fact

that the dyes molecules are in good interaction on the surface of the catalyst at these pH values. The low degradation rate under highly acidic and highly alkaline pH may due to fact that ZnO NPs may undergo photocorrosion through self- oxidation at pH lower than 4. Moreover, In a strongly alkaline environment, ZnO may also undergo dissolution as given in equations 11 to 13 respectively [87].

$$ZnO + 2h^{+} \longrightarrow Zn^{2+} + 1/2O_2 \quad \text{Eq 10}$$

$$ZnO + 2H^{+} \longrightarrow Zn^{2+} + H_2O \quad \text{Eq 11}$$

$$ZnO + H_2O + 2OH^{-} \longrightarrow Zn(OH)_4^{2-} \quad \text{Eq 12}$$

3.10.2 Trapping experiment

To find out the role of dopants on the degradation of dyes, we performed experiments to examine the main reactive species from hydroxyl radical, superoxide radical anion and hole using different scavengers. Therefore, different scavengers were added to the aqueous solution of dyes to investigate the inhibitory effects of scavengers. It is clearly seen from the Fig. 15 that the maximum decomposition of MB dye takes place without any scavenger. However, potassium Iodide (KI) caused highest negative effect on degradation efficiency of dye, indicating that hydroxyl radicals and holes are the major reactive species for decolorization of MB in the presence of Nd-doped ZnO NPs. In addition, the role of hydroxyl radicals was investigated by the addition of isopropyl alcohol (IPA) and the results indicate that the degradation of MB was found to be inhibited significantly. Furthermore, a very small change in degradation of MB is observed after addition of benzoquinone (quencher for superoxide radical anion). The mechanism for trapping of reactive species is given below.

$$I^- + {}^{\bullet}OH \longrightarrow I^{\bullet} + {}^{-}OH \quad \text{Eq 13}$$

$$I^- \longrightarrow I^{\bullet} + e^- \quad \text{Eq 14}$$

$$e^- + h_{vb}^+ \longrightarrow \text{heat} \quad \text{Eq 15}$$

$$I^{\bullet} + I^- \longrightarrow I_2^{\bullet -} \quad \text{Eq 16}$$

$$I_2^{\bullet -} \longrightarrow I_2 + e^- \quad \text{Eq 17}$$

$$IPOH + {}^{\bullet}OH \longrightarrow IPO^{\bullet} + H_2O \quad \text{Eq 18}$$

$$BQ + O_2^{\bullet -} \longrightarrow BQ^{\bullet -} + O_2 \quad \text{Eq 19}$$

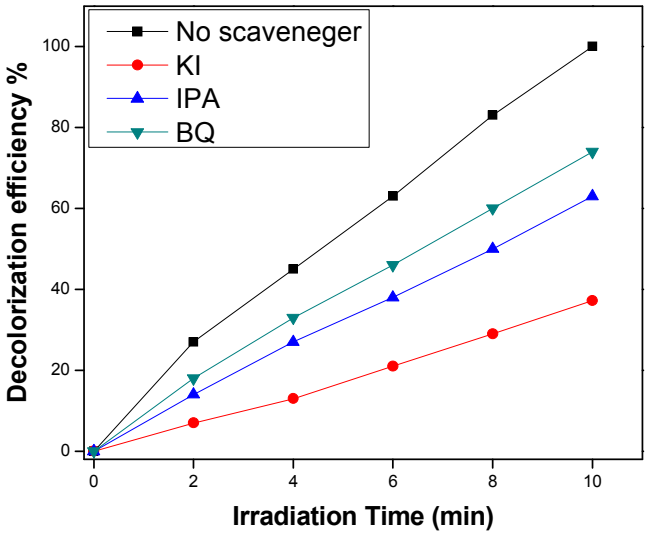

Fig.15. Decolorization efficiency of MB in the presence of different radical scavenger over 2% Nd-doped ZnO under visible light illumination.

3.10.3 Photostability and Reusability of doped ZnO NPs

In addition to photocatalytic performance, the reusability of fabricated photocatalyst is also very important issue for its practical applications. To investigate the stability of hexagonal nanorod, we conduct the four successive photocatalytic experiment for degradation of MB under visible light irradiation in the presence of recycled 2% Nd-

doped ZnO NPs and all other parameters were kept unchanged. Fig. 16 shows that 2% Nd-doped ZnO NPs exhibited effective stability under visible light illumination, however a slight reduction in efficiency from 100% to 95.6% was observed after third cycles. Therefore, synthesized doped ZnO NPs can be an efficient photocatalyst for photoxidation of pollutants with higher reusability potential. Hence, doping of semiconductor with suitable metal ion enhance the stability of photocatalysts [78,83].

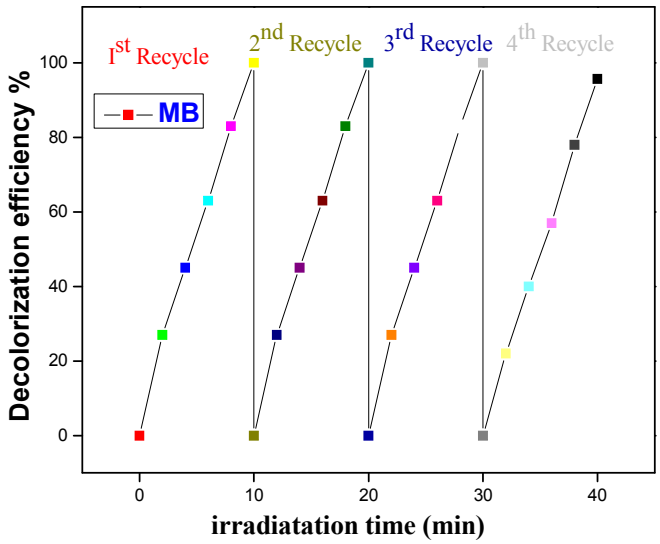

Fig.16. Photostability of 2% Nd-doped ZnO NPs within four consecutive cycles for degradation of MB under visible light illumination.

3.10.4 Mechanism of degradation of dyes

On the basis of above experimental results and previous studies [88] a possible mechanism for degradation of dyes over doped ZnO NPs is shown in scheme 1. The mechanism involved degradation of dyes employing irradiation of ZnO could be visualized as follows. On absorption of photons of energy equal to or greater than its band gap of prepared ZnO NPs, an electron may be promoted from the valence band to the conduction band leaving behind an electron vacancy or ‘‘hole’’ in the valence band. Generally, the photocatalytic degradation of dyes in the presence of bare ZnO was found to be lower than doped materials due to recombination of electron and hole pairs. The enhanced photocatalytic activity of doped ZnO NPs is not only due to that dopants can improve the absorption efficiency of the NPs to solar light but also suppressed the recombination rate

of e/h^+ pairs by trapping the electron, which improved the separation of charge carrier. Furthermore, the higher separation of charge carries in doped ZnO NPs was confirmed by PL spectra. The tarp electron is picked up by oxygen to generate superoxide radical anions. At same time hole generated at the valence band (h^+_{VB}) may react with surface bound H_2O to produce the highly reactive hydroxyl radical. The superoxide radical anions ($^{\bullet}O_2^-$) and hydroxyl radicals ($^{\bullet}OH$) produced under visible light irradiation are responsible for degradation of dyes [89,90].

In addition doped ZnO NPs have small crystallite size therefore possess large surface areas as inferred from BET, TEM and XRD. The photocatalytic activity also depends upon surface area. Larger the surface area higher the activity because increase in surface area leading to adsorption of more pollutants on the surface of ZnO NPs. Hence, the hexagonal rod like doped ZnO NPs reveal efficient photocatalytic activity [91].

On the other hand a dye-sensitized mechanism may also possible as indicated in experiments carried out for degradation of both dyes over pure ZnO NPs under visible light source. Dyes such as MB and RR-241 are also visible light absorbing and get excited in visible light. The excited dye* can transfer the electron to the CB of ZnO NPs [92–94]. The electron can be trapped by dopant at surface or by the impurity band preventing the recombination rate of charge carrier. The trapped electrons may subsequently be transfer to adsorbed oxygen to generate the superoxide radical anion ($O_2^{\bullet-}$) which may act as a strong reducing agent and may form hydrogen peroxide given in following equations. The hydroxyl radical ($^{\bullet}OH$) formed in the reaction mixture may act as a strong oxidizing agent. These ROS are responsible for degradation of dyes and killing of bacterial and cancer cells.

$$dye + \text{Visible Light} \longrightarrow dye^{*} \quad \text{Eq 20}$$

$$\text{Doped ZnO} + \text{Visible Light} \longrightarrow e_{cb}^{-} + h_{vb}^{+} \quad \text{Eq 21}$$

$$dye^{*} + \text{Doped ZnO} \longrightarrow dye^{\bullet +} + e_{cb}^{-} \quad \text{Eq 22}$$

$$Nd/Er^{3+} + e \longrightarrow Nd/Er^{2+} \quad \text{Eq 23}$$

$$Nd/Er^{2+} + O_2 \longrightarrow Nd/Er^{3+} + O_2^{\bullet -} \quad \text{Eq 24}$$

$$e_{cb}^{-} + O_2 \longrightarrow O_2^{\bullet -} \quad \text{Eq 25}$$

$$h_{vb}^{+} + H_2O \longrightarrow {}^{\bullet}OH + H^{+} \quad \text{Eq 26}$$

$$O_2^{\bullet -} + H_2O + 2H^{+} \longrightarrow H_2O_2 + O_2 \quad \text{Eq 27}$$

$$H_2O_2 + e \longrightarrow {}^{-}OH + {}^{\bullet}OH \quad \text{Eq 28}$$

$${}^{\bullet}OH/O_2^{\bullet -} + \text{Absorbed dye/dye}^{\bullet +} \longrightarrow \text{Degradtion products} \quad \text{Eq 29}$$

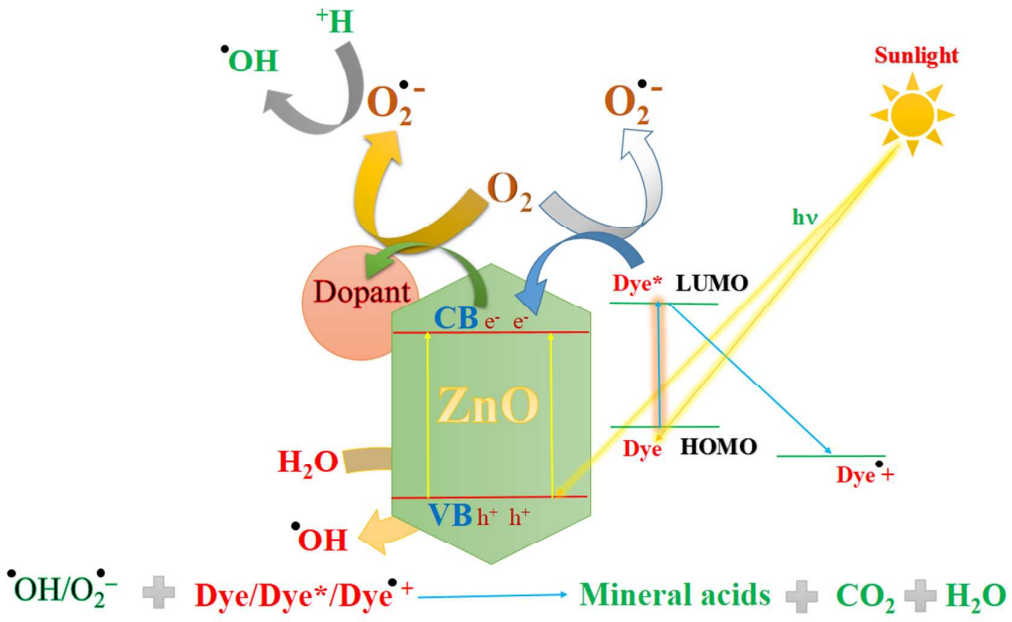

Scheme 1. A plausible mechanism for degradation of dyes using hexagonal nanorod ZnO under visible light irradiation.

4. Conclusion

In summary, we have successfully synthesized the hexagonal pure and Er/Nd doped ZnO nanorods by a simple and facile sol gel method using zinc acetate dihydrate as a precursor. All doped ZnO NPs exhibit smaller crystallite size, red shift in absorbance spectra, which allow utilization of visible light, greater separation of e/h^+ pairs and more adsorption of dyes on the surface of doped ZnO as compare to bare ZnO NPs. The fabricated doped ZnO NPs showed better photocatalytic activity for degradation of MB and RR-241 dyes under visible light. The enhanced photocatalytic activity of doped ZnO NPs may be due to smaller crystalline size and higher surface area. The dopants on the surface may act as electron wells to enhance the charge carrier inferred from EDX, PL, XPS and FTIR. In addition to superb photocatalytic activity and higher photostability doped ZnO also exhibit better anticancer and antibacterial activity than pure ZnO NPs.

Associated Content

Supporting Information (SI)

The supporting information contains the results of following measurements such as X-ray photoelectron spectroscopy (XPS) measurement, Brunauer −Emmett −Teller (BET) measurement, Thermal analysis measurement (TGA and DSC), The plot of $\ln C/C_0$ Vs. irradiation time, Effect of catalyst loading, Effect of pH, Apparent rate constant and R^2 value for degradation of dyes in the presence of doped ZnO NPs.

Acknowledgements:

Financial support to Research Project from Ministry of Mines, Government of India, New Delhi, Alexander von Humboldt foundation, Germany under research group linkage programme and DRS, FIST & PURSE support to the Department of Chemistry, Aligarh Muslim University Aligarh are gratefully acknowledged. We thank Department of Physics, A.M.U, Aligarh for conducting XRD analysis of synthesized materials.

Reference:

1 P. M. Martins, V. Gomez, A. C. Lopes, C. J. Tavares, G. Botelho, S. Irusta and S. Lanceros-Mendez, *J. Phys. Chem. C*, 2014, **118**, 27944–27953.

2 S. Singh, V. Srivastava and I. Mall, *J. Phys. Chem. C*, 2013, **117**, 15229–15240.

3 R. Ahlawat and V. Srivastava, *CLEAN–Soil, Air, Water*, 2008, **36**, 863–869.

4 A. Khataee, R. Darvishi Cheshmeh Soltani, Y. Hanifehpour, M. Safarpour, H. Gholipour Ranjbar and S. W. Joo, *Ind. Eng. Chem. Res.*, 2014, **53**, 1924–1932.

5 A. R. K. and S. H. A. Rezaee, H. Masoumbeigi, R. D. C. Soltani, *Desalin. Water Treat.*, 2012, **44**, 174–179.

6 X. Guo, W. Song, C. Chen, W. Di and W. Qin, *Phys. Chem. Chem. Phys.*, 2013, **15**, 14681–14688.

7 E. Casbeer, V. Sharma and X. Li, *Sep. Purif. Technol.*, 2012, **87**, 1–14.

8 J. Zhang, K. Yu, Y. Yu, L.-L. Lou, Z. Yang, J. Yang and S. Liu, *J. Mol. Catal. A Chem.*, 2014, **391**, 12–18.

9 X. Chen and S. Mao, *Chem. Rev.*, 2007, **107**, 2891–2959.

10 R. Kozhummal, Y. Yang, F. Güder, A. Hartel, X. Lu, U. M. Küçükbayrak, A. Mateo-Alonso, M. Elwenspoek and M. Zacharias, *ACS Nano*, 2012, **6**, 7133–41.

11 J. Mu, C. Shao, Z. Guo, Z. Zhang, M. Zhang, P. Zhang, B. Chen and Y. Liu, *ACS Appl. Mater. Interfaces*, 2011, **3**, 590–596.

12 P. V Korake, R. S. Dhabbe, A. N. Kadam, Y. B. Gaikwad and K. M. Garadkar, *J. Photochem. Photobiol. B.*, 2014, **130**, 11–9.

13 P. Gomathisankar, K. Hachisuka, H. Katsumata, T. Suzuki, K. Funasaka and S. Kaneco, *ACS Sustain. Chem. Eng.*, 2013, **1**, 982–988.

14 B. Cao and W. Cai, *J. Phys. Chem. C*, 2008, **112**, 680–685.

15 W. Raza, M. M. Haque and M. Muneer, *Appl. Surf. Sci.*, 2014, **322**, 215–224.

16 W. Han, L. Ren, X. Qi, Y. Liu, X. Wei, Z. Huang and J. Zhong, *Appl. Surf. Sci.*, 2014, **299**, 12–18.

17 T. Xu, L. Zhang, H. Cheng and Y. Zhu, *Appl. Catal. B Environ.*, 2011, **101**, 382–387.

18 B. Li and H. Cao, *J. Mater. Chem.*, 2011, **21**, 3346–3349.

19 L. Zhang, L. Du, X. Yu, S. Tan, X. Cai, P. Yang, Y. Gu and W. Mai, *ACS Appl. Mater. Interfaces*, 2014, **6**, 3623–3629.

20 Z. Liu, C. Liu, J. Ya and E. Lei, *Renew. Energy*, 2011, **36**, 1177–1181.

21 L. Arun Jose, J. Mary Linet, V. Sivasubramanian, A. K. Arora, C. Justin Raj, T. Maiyalagan and S. Jerome Das, *Mater. Sci. Semicond. Process.*, 2012, **15**, 308–313.

22 J.-W. Lo, W.-C. Lien, C.-A. Lin and J.-H. He, *ACS Appl. Mater. Interfaces*, 2011, **3**, 1009–1014.

23 B. Subash, B. Krishnakumar, M. Swaminathan and M. Shanthi, *Langmuir*, 2013, **29**, 939–49.

24 G. H. Mhlongo, O. M. Ntwaeaborwa, H. C. Swart, R. E. Kroon, P. Solarz, W.

Ryba-Romanowski and K. T. Hillie, *J. Phys. Chem. C*, 2011, **115**, 17625–17632.

25 H. Serier, M. Gaudon and M. Ménétrier, *Solid State Sci.*, 2009, **11**, 1192–1197.

26 F. Meng, J. Yin, Y.-Q. Duan, Z.-H. Yuan and L.-J. Bie, *Sensors Actuators B Chem.*, 2011, **156**, 703–708.

27 W.-H. Zhang, W.-D. Zhang and J.-F. Zhou, *J. Mater. Sci.*, 2009, **45**, 209–215.

28 S. Du, Y. Tian, H. Liu, J. Liu and Y. Chen, *J. Am. Ceram. Soc.*, 2006, **89**, 2440–2443.

29 S. Suwanboon, P. Amornpitoksuk and P. Bangrak, *Ceram. Int.*, 2011, **37**, 333–340.

30 H. Wang, C. Li, H. Zhao, R. Li and J. Liu, *Powder Technol.*, 2013, **239**, 266–271.

31 R. Saleh and N. F. Djaja, *Superlattices Microstruct.*, 2014, **74**, 217–233.

32 C. Pérez, A. M. Agnese and J. L. Cabrera, *J. Ethnopharmacol.*, 1999, **66**, 91–96.

33 T. Mosmann, *J. Immunol. Methods*, 1983, **65**, 55–63.

34 F.-X. Xiao, *ACS Appl. Mater. Interfaces*, 2012, **4**, 7055–63.

35 P. Zhang, B. Li, Z. Zhao, C. Yu, C. Hu, S. Wu and J. Qiu, *ACS Appl. Mater. Interfaces*, 2014, **6**, 8560–6.

36 R. Kumar, S. Anandan, K. Hembram and T. N. Rao, *ACS Appl. Mater. Interfaces*, 2014, **6**, 13138–48.

37 Z. Zhang, C. Shao, X. Li, C. Wang, M. Zhang and Y. Liu, *ACS Appl. Mater. Interfaces*, 2010, **2**, 2915–23.

38 L. Zhu, M. Zhi, Z. Ye and B. Zhao, *Appl. Phys. Lett.*, 2006, **88**, 113106.

39 J. Rao, A. Yu, C. Shao and X. Zhou, *ACS Appl. Mater. Interfaces*, 2012, **4**, 5346–52.

40 H. Kleinwechter, C. Janzen, J. Knipping, H. Wiggers and P. Roth, *J. Mater. Sci.*, 2002, **37**, 4349–4360.

41 X. Q. Wei, Z. G. Zhang, M. Liu, C. S. Chen, G. Sun, C. S. Xue, H. Z. Zhuang and B. Y. Man, *Mater. Chem. Phys.*, 2007, **101**, 285–290.

42 L. Loh, J. Briscoe and S. Dunn, *ACS Appl. Mater. Interfaces*, 2015, **7**, 152–7.

43 N. Rajeswari Yogamalar and A. Chandra Bose, *J. Solid State Chem.*, 2011, **184**, 12–20.

44 C. K. Ghosh, S. R. Popuri, T. U. Mahesh and K. K. Chattopadhyay, *J. Sol-Gel Sci. Technol.*, 2009, **52**, 75–81.

45 S. K. Chaturvedi, E. Ahmad, J. M. Khan, P. Alam, M. Ishtikhar and R. H. Khan, *Mol. Biosyst.*, 2015, **11**, 307–16.

46 D. Barpuzary and M. Qureshi, *ACS Appl. Mater. Interfaces*, 2013, **5**, 11673–82.

47 H. Qin, W. Li, Y. Xia and T. He, *ACS Appl. Mater. Interfaces*, 2011, **3**, 3152–6.

48 N. Udawatte, M. Lee, J. Kim and D. Lee, *ACS Appl. Mater. Interfaces*, 2011, **3**, 4531–8.

49 M. A. Butler, *J. Appl. Phys.*, 1977, **48**, 1914.

50 R. K. Gupta, K. Ghosh and P. K. Kahol, *Phys. E Low-dimensional Syst. Nanostructures*, 2009, **41**, 617–620.

51 M. Khatamian, A. A. Khandar, B. Divband, M. Haghighi and S. Ebrahimiasl, *J. Mol. Catal. A Chem.*, 2012, **365**, 120–127.

52 Y. Zhou, S. X. Lu and W. G. Xu, *Environ. Prog. Sustain. Energy*, 2009, **28**, 226–233.

53 B. Shahmoradi, K. Soga, S. Ananda, R. Somashekar and K. Byrappa, *Nanoscale*, 2010, **2**, 1160–1164.

54 R. John and R. Rajakumari, *Nano-Micro Lett.*, 2012, **4**, 65–72.

55 A. S. H. Hameed, et al, *Sci. Rep.*, 2016, **6**, doi:10.1038/srep24312.

56 R. John and R. Rajakumari, *Nano-Micro Lett.*, 2012, **4**, 65–72.

57 S. D. Senol, *J. Mater. Sci. Mater. Electron.*, 2016, DOI 10.1007/s10854–016–4765–1.

58 Q. Deng, X. Duan, D. H. L. Ng, H. Tang, Y. Yang, M. Kong, Z. Wu, W. Cai and G. Wang, *ACS Appl. Mater. Interfaces*, 2012, **4**, 6030–6037.

59 M. Caglar and F. Yakuphanoglu, *Appl. Surf. Sci.*, 2012, **258**, 3039–3044.

60 Z. L. Wang, X. Y. Kong, Y. Ding, P. Gao, W. L. Hughes, R. Yang and Y. Zhang, *Adv. Funct. Mater.*, 2004, **14**, 943–956.

61 J. H. Zheng, J. L. Song, Z. Zhao, Q. Jiang and J. S. Lian, *Cryst. Res. Technol.*, 2012, **47**, 713–718.

62 C. Ren, B. Yang, M. Wu, J. Xu, Z. Fu, Y. Lv, T. Guo, Y. Zhao and C. Zhu, *J. Hazard. Mater.*, 2010, **182**, 123–129.

63 L. Armelao, G. Bottaro, M. Pascolini, M. Sessolo, E. Tondello, M. Bettinelli and A. Speghini, *J. Phys. Chem. C*, 2008, **112**, 4049–4054.

64 Y. Z. Z Zhang, XL Zhong, H Liao, F Wang, JB Wang, *Appl. Surf. Sci.*, 2011, **257**, 7461–7465.

65 S. Huang, L. Gu, C. Miao, Z. Lou, N. Zhu, H. Yuan and A. Shan, *J. Mater. Chem. A*, 2013, **1**, 7874.

66 L. Armelao, D. Barreca, G. Bottaro, A. Gasparotto, D. Leonarduzzi, C. Maragno, E. Tondello and C. Sada, *J. Vac. Sci. Technol. A Vacuum, Surfaces, Film.*, 2006, **24**, 1941–1947.

67 W. C. Lang, B. D. Padalia, L. M. Watson, D. J. Fabian and P. R. Norris, *Faraday Discuss. Chem. Soc.*, 1975, **60**, 37–43.

68 L. Chen, D. Jiang, T. He, Z. Wu and M. Chen, *CrystEngComm*, 2013, **15**, 7556.

69 D. Zhang, M. Wen, B. Jiang, G. Li and J. C. Yu, *J. Hazard. Mater.*, 2012, **211-212**, 104–11.

70 J. Cao, B. Xu, H. Lin, B. Luo and S. Chen, *Chem. Eng. J.*, 2012, **185-186**, 91–99.

71 B. Panigrahy, M. Aslam, D. S. Misra and D. Bahadur, *CrystEngComm*, 2009, **11**, 1920.

72 D. E. Motaung, G. F. Malgas, C. J. Arendse and S. E. Mavundla, *Mater. Chem. Phys.*, 2012, **135**, 401–410.

73 K. J. Chen, T. H. Fang, F. Y. Hung, L. W. Ji, S. J. Chang, S. J. Young and Y. J. Hsiao, *Appl. Surf. Sci.*, 2008, **254**, 5791–5795.

74 P. S. Sokolov, A. N. Baranov, Z. V. Dobrokhotov and V. L. Solozhenko, *Russ.*

Chem. Bull., 2010, **59**, 325–328.

75 R. Brayner, R. Ferrari-Iliou, N. Brivois, S. Djediat, M. F. Benedetti and F. Fiévet, *Nano Lett.*, 2006, **6**, 866–70.

76 L. Zhang, Y. Jiang, Y. Ding, M. Povey and D. York, *J. Nanoparticle Res.*, 2006, **9**, 479–489.

77 A. Lipovsky, Z. Tzitrinovich, H. Friedmann, G. Applerot, A. Gedanken and R. Lubart, *J. Phys. Chem. C*, 2009, **113**, 15997–16001.

78 P. K. Sanoop, S. Anas, S. Ananthakumar, V. Gunasekar, R. Saravanan and V. Ponnusami, *Arab. J. Chem.*, 2012.

79 A. R. Khataee, Y. Hanifehpour, M. Safarpour, M. Hosseini and S. W. Joo, *Sci. Adv. Mater.*, 2013, **5**, 1074–1082.

80 W. Raza, M. M. Haque, M. Muneer, M. Fleisch, A. Hakki and D. Bahnemann, *J. Alloys Compd.*, 2015, **632**, 837–844.

81 W. Raza, M. M. Haque, M. Muneer, T. Harada and M. Matsumura, *J. Alloys Compd.*, 2015, **648**, 641–650.

82 M. M. Haque, W. Raza, A. Khan and M. Muneer, *J. Nanoeng. Nanomanufacturing*, 2014, **4**, 135–139.

83 W. Raza, M. M. Haque, M. Muneer and D. Bahnemann, *Arab. J. Chem.*, 2015, http://dx.doi.org/10.1016/j.arabjc.2015.09.002.

84 W. Raza, A. Khan, U. Alam, M. Muneer and D. Bahnemann, *J. Mol. Struct.*, 2016, **1107**, 39–46.

85 S. Kansal, N. Kaur and S. Singh, *Nanoscale Res. Lett.*, 2009, **4**, 709–16.

86 B. Krishnakumar, B. Subash and M. Swaminathan, *Sep. Purif. Technol.*, 2012, **85**, 35–44.

87 R. Comparelli, E. Fanizza, M. L. Curri, P. D. Cozzoli, G. Mascolo and A. Agostiano, *Appl. Catal. B Environ.*, 2005, **60**, 1–11.

88 H. Qin, W. Li, Y. Xia and T. He, *ACS Appl. Mater. Interfaces*, 2011, **3**, 3152–6.

89 S. A. Ansari, M. M. Khan, J. Lee and M. H. Cho, *J. Ind. Eng. Chem.*, 2014, **20**, 1602–1607.

90 C. Chen, Y. Zheng, Y. Zhan, X. Lin, Q. Zheng and K. Wei, *Dalton Trans.*, 2011, **40**, 9566–70.

91 L. Zhang, L. Yin, C. Wang, N. Lun and Y. Qi, *ACS Appl. Mater. Interfaces*, 2010, **2**, 1769–73.

92 T. Wu, G. Liu, J. Zhao, H. Hidaka and N. Serpone, *J. Phys. Chem. B*, 1998, **102**, 5845–5851.

93 A. Hagfeldt and M. Graetzel, *Chem. Rev.*, 1995, **95**, 49–68.

94 S. Rehman, R. Ullah, A. M. Butt and N. D. Gohar, *J. Hazard. Mater.*, 2009, **170**, 560–9.

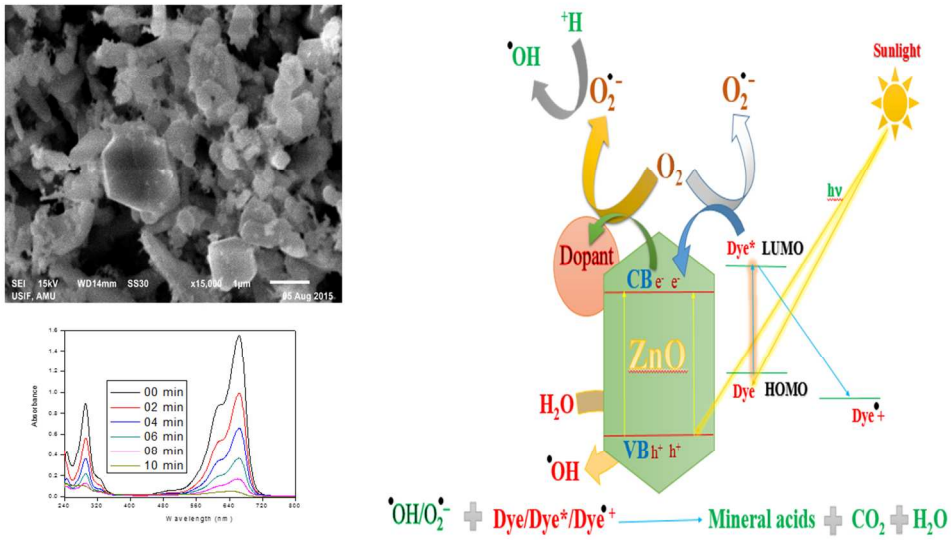

338x190mm (96 x 96 DPI)